Spatial vector characterization of intra-particle pore structures for carbonate sand particles

Yi-Hang Wu,[1] Bei-Bing Dai, Ph.D.,[2] Yi-Pik Cheng, Ph.D.,[3] Jun Yang, Ph.D., F.ASCE[4]

[1]Ph.D. student, School of Civil Engineering, Sun Yat-sen University, Guangzhou, China, 510275; and Department of Civil, Environmental and Geomatic Engineering, University College London, London, United Kingdom, WC1E 6BT; E-mail: wuyh239@mail2.sysu.edu.cn

[2]Professor, School of Civil Engineering, Sun Yat-sen University, Guangzhou, China, 510275; State Key Laboratory for Tunnel Engineering, Guangzhou, China, 510275; and Southern Marine Science and Engineering Guangdong Laboratory (Zhuhai), Zhuhai, China, 519082; E-mail: daibb@mail.sysu.edu.cn (Corresponding author)

[3]Associate professor, Department of Civil, Environmental and Geomatic Engineering, University College London, London, United Kingdom, WC1E 6BT; E-mail: yi.cheng@ucl.ac.uk

[4]Professor, Department of Civil Engineering, The University of Hong Kong, Hong Kong, China, 999077; E-mail: junyang@hku.hk

Abstract

This paper presents an investigation of the spatial distribution of intra-particle voids in carbonate sand particles using X-ray micro-tomography (μCT) to obtain high-resolution 3D particle images. A vector representation approach is introduced within a statistical micromechanics framework to characterize the spatial organization of internal pore structures. The study establishes a tensor formulation based on pore orientation vectors and volume-weighted pore orientation vectors to quantify the anisotropic distribution of intra-particle pores. It is found that volume-weighted pore orientation vectors exhibit a considerably higher degree of anisotropy than pure pore orientation vectors. For highly porous particles, the anisotropic distribution of volume-weighted pore orientation vectors is largely governed by the presence of a dominant open pore, aligning the principal pore anisotropy direction with the overall particle orientation. Moreover, a dependence of porosity, pore diameter, and the anisotropy parameter a_v on particle size is observed, while the pore shape parameter (aspect ratio) remains size-independent. The relationships between pore structure characteristics and particle skeleton morphology are explored, revealing that correlations, such as those between sphericity, porosity, and pore anisotropy, are not strictly interdependent, depending on factors like pore connectivity and size. These findings provide new insights into the micromechanical behavior of carbonate sand particles and their influence on hydraulic transport properties.

Keywords: carbonate sands; internal pores; spatial distribution; anisotropy; X-ray μCT; vector representation

1. Introduction

Carbonate sands are a kind of natural sands derived from marine biological remnants (e.g., corals, mollusk, foraminifera, ooidic and so on) (Coop 1990), which are commonly encountered in offshore engineering construction. The special cavity structure of marine organisms allows carbonate sand particles to retain considerable internal pores and exhibit different mechanical properties from terrestrial silica sand particles (Dong et al. 2024; Giretti et al. 2018; Zhang et al. 2023). The characterization of the internal pore structures, along with their relations with the particle breakage and other mechanical behavior, has garnered increasing attention from researchers (Andò et al. 2013; Fonseca et al. 2012; Karatza et al. 2018).

For example, Li et al. (2020) observed through in situ micro-CT that the presence of internal pores facilitates the initiation and propagation of cracks, contributing to the reduction of particle failure strength. Lv et al. (2021) used the index of porosity to characterize the overall pore volume within a single particle, and found that particles almost completely lose their strength and stiffness when the porosity exceeds 0.25 in the single-particle compression test. Kuang et al. (2024) employed the porosity and pore fractal dimension to describe the pore characteristic of porous particles in the discrete element method (DEM) simulations, revealing that as these pore descriptors increase, the particle failure mode transits from being brittle to being ductile. Zhou et al. (2020) conducted a comprehensive investigation on the pore size distribution, pore fractal dimension, and the Euler characteristic, and developed the correlation between the pore characteristic indexes and the permeability property. It is obvious that researchers have made significant achievements in characterizing the internal pore structures of carbonate sand particles (e.g., the pore size, pore shape, fractal dimension of pore size distribution, and pore connectivity) and correlating the pore characteristics with the mechanical behavior of sand particles or assemblies (Fan et al. 2021; He et al. 2021; Kong and Fonseca 2018; Zhou et al. 2020). However, it seems that in these studies, the scalar parameters are preferred for the characterization of internal pore structures, which cannot capture the spatial distribution characteristics of pore structures.

Recently, Zhao et al. (2015) has observed through the single-particle compression test that the spatial location of weak points (i.e., the internal pores and impurities) in a particle plays an important role in determining the crack initiation and propagation path, as well as the particle fracture mode. Similarly, Zhou et al. (2022), using the numerical simulation based on a combined finite-discrete element method (FDEM), found that a specific location where an intra-particle pore is present tends to suffer from an intense stress concentration, which is mainly responsible for the initiation and progression of cracks. In addition, Ma et al. (2021) revealed that varying the pore orientations leads to the variation of the permeability levels, even under an identical pore volume. Such studies have clearly demonstrated that the spatial distribution of internal pore structures can exert an unignorable effect on the mechanical behavior (e.g., the particle breakage and permeability) of carbonate sand particles. It is also noted that the current method of characterizing the pore structures within particles based on the scalar representation cannot thoroughly describe the spatial distribution characteristics, which has limited a comprehensive and accurate understanding of the mechanical behavior of carbonate sands.

In this context, this study focuses on the characterization of three-dimensional spatial distribution of internal pores in carbonate sand particles, with the use of a vector representation approach. By a careful microscopic analysis of μCT images, the pore structures are characterized by the pore orientation vector and volume-weighted pore orientation vector in a three-dimensional space. On the basis of vector quantities, a statistical analysis is done to achieve a micromechanical description of internal pore structures in a 3D space. Efforts are also made to investigate the relationship between the pore and solid phase characteristics. It is hoped that this study can provide some new insights into the internal pore structure of carbonate sands.

2. Soil description and digital implementation

2.1 Test material and methodology

The carbonate sand particles under investigation are a kind of calcareous sediments primarily originating from corals in the South China Sea. The equivalent diameter (D_e) of the sand particles ranges from 0.3 mm to 8.2 mm (see Fig .1), which is given by $D_e = (6V_s/\pi)^{1/3}$, where V_s is the volume of the particle. The particle structures for both the solid and pore phases, were examined using a μCT system (NanoVoxel 3000) from Sanying Precision Instruments Co., Ltd.

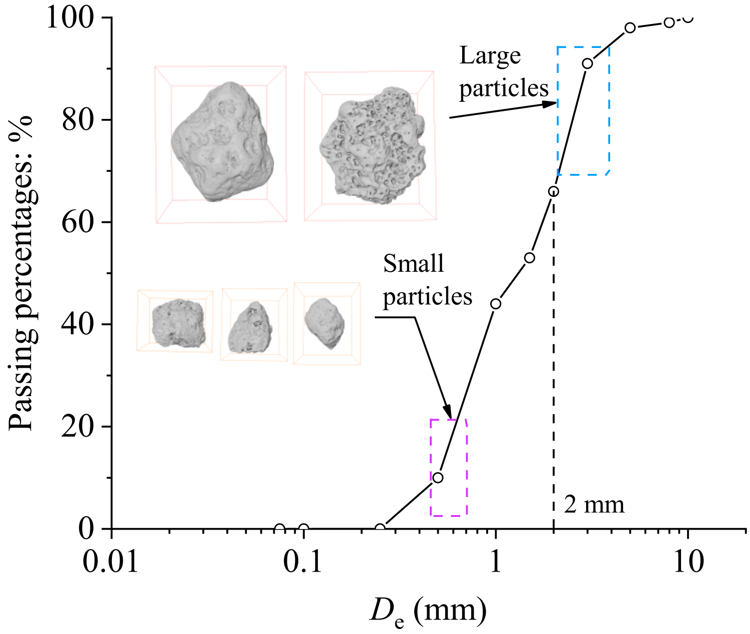

Fig. 1 The particle gradation of carbonate sand particles for testing

2.2 Image processing

For the processing of raw image data obtained from scanning, a 3D median filtering algorithm was employed to reduce the noise generated during scanning. The voxels corresponding to the solid phase were initially identified using Otsu's thresholding segmentation method (Otsu 1979), which determines the optimal threshold value by maximizing the variance between distinct phases in grayscale images. This method has been widely recognized for its effectiveness in distinguishing different phases in CT-reconstructed images (Nishimura et al. 2024; Zhao et al. 2015). Subsequently, the pore phase was determined through the application of filling algorithms, including the Fill Holes and Ambient Occlusion algorithms. According to the classification method proposed by Rouquerol et al. (1994), the internal pores within the particle boundary consist of two components: closed pores and open pores. The Fill Holes algorithm helps to identify pore voxels surrounded by the solid-phase voxel structure as closed pores (Cheng and Wang 2021; Zhou et al. 2022). The Ambient Occlusion algorithm is used to extract open pores based on the occlusion values of light rays projected from multiple angles (Titschack et al. 2018). Using these image processing methods, the voxel sets for both the solid skeleton and pores were extracted, enabling a further analysis of their size and morphology. The particle and pore volumes are computed by summing the volumes of all corresponding image voxels. While closed pores typically exhibit a spherical or ellipsoidal shape, a big open pore often presents as an inter-connected nest-like unit of pore volume for particles with high porosity, as shown in the subset of Fig. 2, and the size of this cluster is represented by its equivalent diameter mentioned above. Previous studies have shown that the two-dimensional pore shape and orientation can be well captured using the ellipses equivalent to the pore outlines (Gao et al. 2020; Zheng et al. 2022). Similar approach was adopted in this study to capture the pore dimensions, with the pores treated as ellipsoids, and some examples for the reconstructed particles and pores are shown in Fig. 2(b). The orientation of the global shape of each pore is determined using the moment of inertia method. The orientation of a pore is represented by a three-dimensional unit vector (see Fig. 2), parallel to the pore's longest axis. This longest axis is treated as its principal axis of inertia, characterized by the eigenvector associated with the largest eigenvalue of the inertia matrix. The dimensions of each particle and pore are determined by the bounding box method, with major (L), intermediate (I) and minor (S) dimensions defined following $L > I > S$ (Huang et al. 2023; Krumbein 1941; Ma et al. 2019). In present study, two morphology parameters, the flatness (FL) and elongation (EL), are calculated, with FL defined as = I/L and EL as S/I. The sphericity (S), describing the degree to which a particle/pore resembles a sphere, is also used to provide a more comprehensive characterization of morphology, and calculated by $S = (36V_s^2)^{1/3}/A$, where A is the surface area of a given particle/pore.

3. Quantifying pore fabric

Fabric tensor has been used to describe the spatial distribution of the vector quantities characterizing the microscopic structures and force network in a granular assembly, such as the contact normal/force vector, branch vector, and particle orientation vector (Fonseca et al. 2013; Ma et al. 2014; Sitharam et al. 2009; Sun and Zheng 2019; Zhao et al. 2021; Zhou and Xu 2024). Note that unlike the almost continuous void spaces in particle assemblies, the internal pores within a single particle can be regarded as a kind of discontinuities. In a 3D space, the orientation vector of an internal pore, denoted as $\vec{n}$ as indicated in Fig. 2, is described by the horizontal angle (α) and the vertical angle (β). Based on the fabric tensor proposed by Satake (1982) and Ken-Ichi (1984), the 3D spatial distribution anisotropy of the intra-particle pores is expressed as

$$\Phi_{ij} = \frac{1}{4\pi}\int_{\Omega} P(\mathbf{n}) n_i n_j \mathrm{d}\Omega \tag{1}$$

where n_i (i=1, 2, 3) is the unit vector of pore orientation, Ω refers to the representative elemental volume (REV), and $P(\mathbf{n})$ is the distribution probability density function. The discrete form of this equation is written as

$$\Phi_{ij} = \frac{1}{N_v}\sum_{N_v} n_i n_j \tag{2}$$

where N_v is the total number of vectors in a particle, and Φ_{ij} is the fabric tensor for the pore orientations. The probability density function $P(\mathbf{n})$ is expressed as a second-order Fourier series (Guo and Zhao 2013; Ouadfel and Rothenburg 2001; Zhao et al. 2018):

$$P(\mathbf{n}) = \frac{1}{4\pi}\left(1 + a_{ij}^{p} n_i n_j\right) \quad (3)$$

where a_{ij}^{p} is a deviatoric and symmetric second-order tensor for the characterization of pore orientation anisotropy. With the substitution of Eq. (3) into Eq. (1), one can obtain

$$a_{ij}^{p} = \frac{15}{2}\Phi'_{ij} \quad (4)$$

where Φ'_{ij} is the deviatoric part of Φ_{ij}, with $\Phi'_{ij} = \Phi_{ij} - \delta_{ij}\Phi_{kk}/3$ (δ_{ij} is the Kronecker delta).

Note that the distribution of pore volumes in a particle is not uniform; the pores with a larger volume may have a more significant impact on the pore anisotropic distribution. With the consideration of pore volume effect, the volume-weighted pore orientation tensor and the probability distribution function are given as

$$\psi_{ij} = \frac{1}{4\pi}\int_{\Omega} V(\mathbf{n}) n_i n_j \mathrm{d}\Omega = \frac{1}{N_v}\sum_{Nv} \frac{v_p n_i n_j}{1 + a_{kl}^{p} n_k n_l} \quad (5)$$

$$V(\mathbf{n}) = \bar{v}_0 (1 + a_{ij}^{v} n_i n_j) \quad (6)$$

The deviatoric tensor related to the anisotropic distribution of volume-weighted pore orientation vectors, a_{ij}^{v}, is defined as

$$a_{ij}^{v} = \frac{15}{2}\frac{\psi'_{ij}}{\bar{v}_0} \quad (7)$$

where $\bar{v}_0$ ($\bar{v}_0 = \psi_{ii}$) is the average pore volume over the entire REV domain with the pore orientation vectors given equal weight at various directions, and this differs from the average volume over all pores.

The invariants of the deviatoric tensor are conventionally used to quantify the degree of the distribution anisotropy for the pore orientation vector and volume-weighted pore orientation vector, which is given by a unified expression:

$$a_* = \sqrt{\frac{3}{2} a_{ij}^* a_{ij}^*} \tag{8}$$

where the sub/super-script * indicates either the pore orientation anisotropy (p) or the volume-weighted pore orientation anisotropy (v).

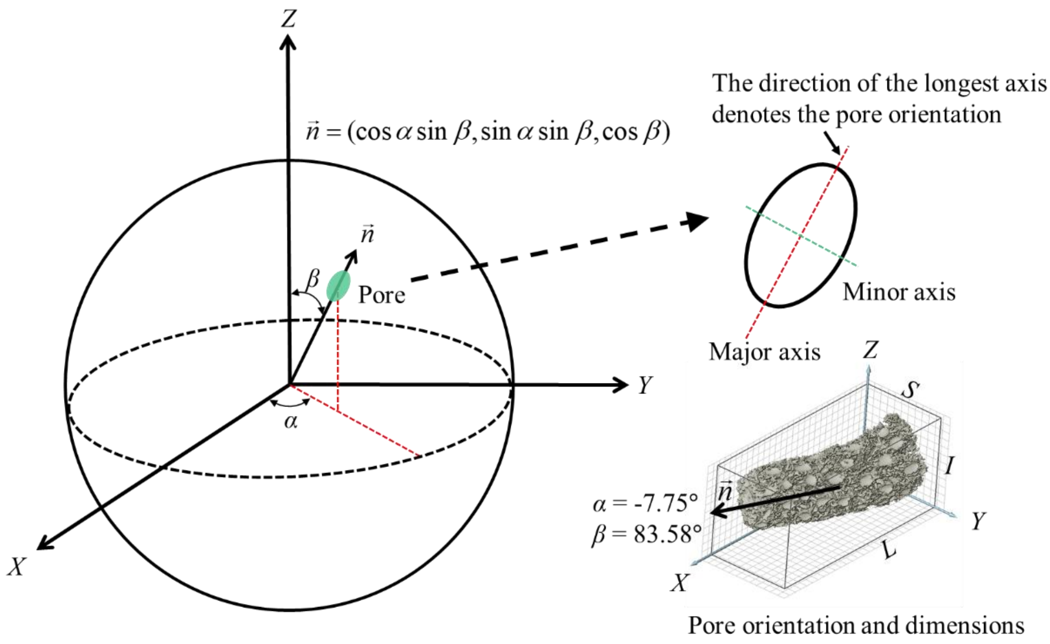

(a)

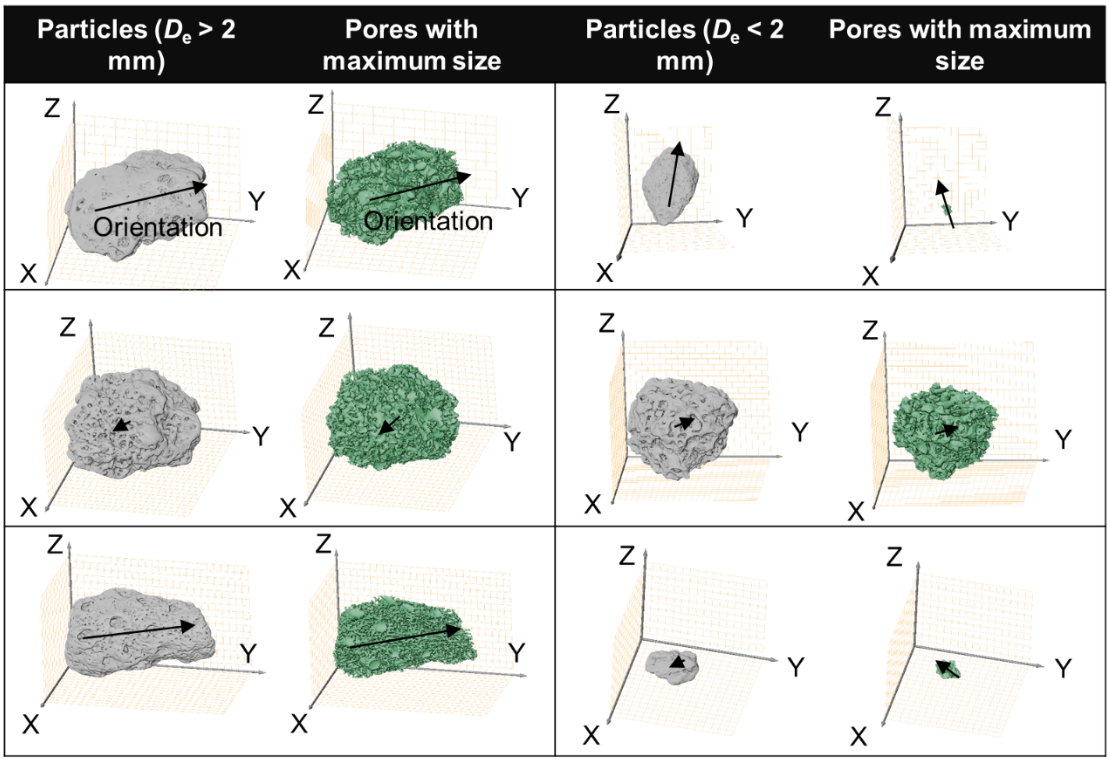

(b)

Fig. 2 (a) Definition of the vector $\vec{n}$ in a unit sphere and (b) examples of reconstructed particles and pores with schematic directional arrows

4. Results and analyses

4.1 Scalar characterization of internal pores

The scalar quantity, porosity (φ), is used here to characterize the volume fraction of the intra-particle pores (including open pores and closed pores) within a particle, which is defined as

$$\varphi = \frac{V_p}{V_p + V_s} \tag{9}$$

where V_p and V_s are the voxel volumes for the pore and solid phases, respectively. Fig. 3 illustrates the density distribution of particle porosity along with the fitting curves given by the Johnson distribution and the normal distribution functions. It is observed that the particles with a higher porosity exhibit a lower occurrence probability. Both Gaussian and Johnson distribution functions were employed to evaluate the distribution curves. The Gaussian distribution is a commonly used symmetric distribution function, while the Johnson distribution is well-suited for handling asymmetric cases. The fitting curve of the Johnson distribution yields similar results but has a slightly higher R^2 value, compared to the normal distribution. The probability density function (PDF) for the Johnson distribution is given by Johnson (1949) as

$$P(x) = \frac{\delta}{\lambda\sqrt{2\pi}\sqrt{1+\left(\frac{x-\xi}{\lambda}\right)^2}} e^{-\frac{1}{2}\left(\gamma+\delta\sinh^{-1}\left(\frac{x-\xi}{\lambda}\right)\right)^2} \quad (10)$$

where ξ, δ, λ, and γ are the function parameters with their values listed in Table 1. Additionally, the particles with an equivalent diameter (D_e) greater than 2 mm tend to have a higher porosity than the smaller particles. Fig. 4(a) presents the relationship between the maximum pore size and the porosity. The normalized maximum pore size ($d_{e,n}$) is defined as the ratio of the maximum equivalent pore diameter against the equivalent diameter for the solid particle skeleton. A clear correlation is identified: $d_{e,n}$ increases as a power function with the increasing porosity, indicating that the particles having a higher porosity are prone to have larger pores that occupy a significant portion of the total particle volume. Some of the particles have a $d_{e,n}$ up to 0.9. In such cases, the particles would be highly hollow, with pore volumes approaching the size of the particles themselves. It can be particularly observed in Fig. 4(b), where some data points for maximum pore size lie close to the diagonal.

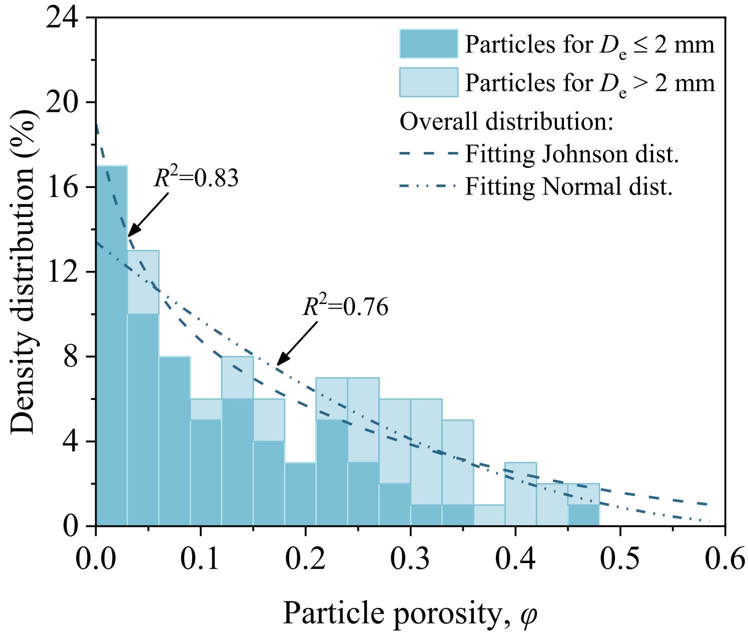

Fig. 3 Distribution of porosity for the tested carbonate sand particles

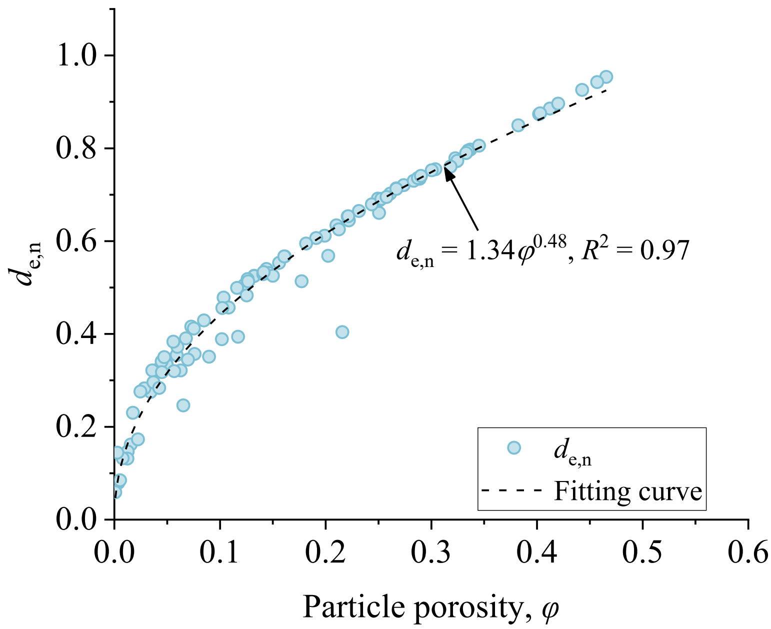

(a)

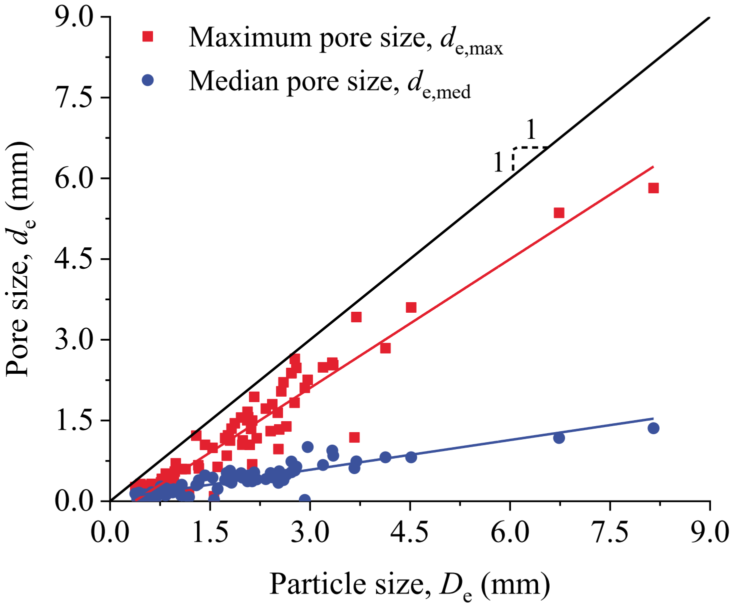

(b)

Fig. 4 (a) Relationship between $d_{e,n}$ and φ for the tested carbonate sand particles, and (b) maximum and median pore size against particle size

Fig. 5 shows the density distribution in terms of pore size and pore shape. The median equivalent diameter, d_{e50}, is used to present a statistical average of the overall pore size in a particle and is calculated by the median value of the cumulative pore size distribution curve. In Fig. 5(a), the Johnson and Gaussian distributions are separately fitted to the data for particles larger and smaller than 2 mm, respectively. It is shown that pore size is positively correlated with particle size, which further supports the observation that larger particles are more prone to breakage (Hardin 1985; Wu et al. 2024). Figure 5(b) reveals that pore shape does not exhibit a clear dependence on particle size, as the aspect ratio of pores exhibits no significant variation across different particle size ranges. For such nearly symmetrical data, the normal distribution function provides a better fit compared to the Johnson distribution.

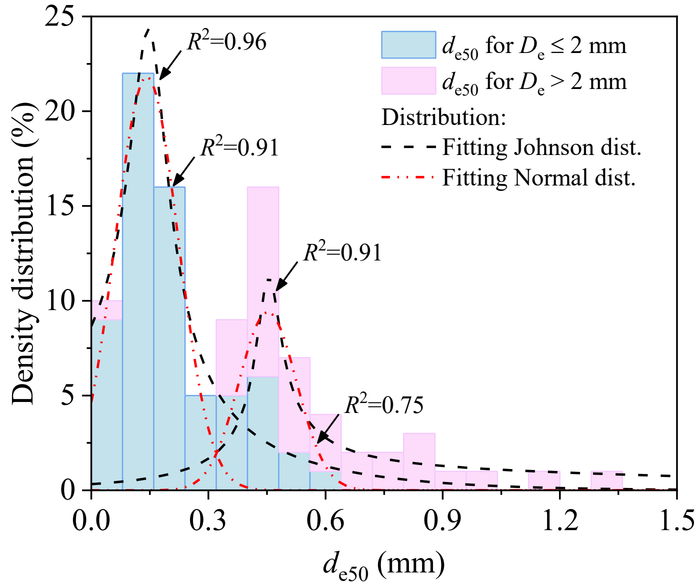

(a)

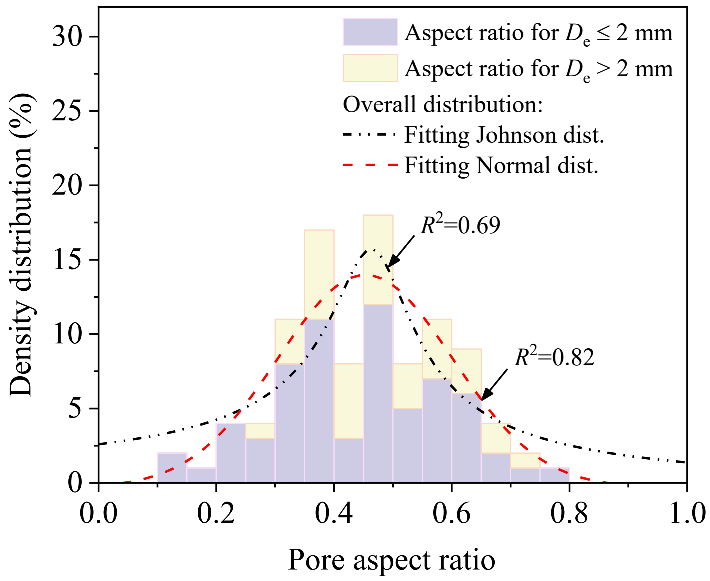

(b)

Fig. 5 Distribution of (a) pore size and (b) pore shape for the carbonate sand particles

4.2 Vector characterization of pore orientations

In this section, the pore orientation is brought into focus for a good understanding of the pore spatial distribution in carbonate sand particles with varying porosities. For an effective characterization of pore orientations in a 3D space, the particle orientations are ensured to align with the Z-axis in the global Cartesian coordinate system through rotating the coordinate system by an angle θ_r, as depicted in Fig. 6. Fig. 7 presents the distributions of pore orientations for four representative carbonate sand particles with the porosity ranging from 1.2% to 22.1%. The particle with a porosity of 1.2% exhibits a relatively isotropic distribution in terms of both the pore orientation and volume-weighted pore orientation vectors, as compared with the particles with high porosities. As the porosity increases, the distribution anisotropy seems to become more pronounced, particularly for the volume-weighted pore orientation vectors, and this is primarily due to the presence of a certain number of large pores that could dominate the overall volume and anisotropic distribution of intra-particle voids. While the pore orientation and volume-weighted pore orientation vectors in the low-porosity particle basically display similar angles for the principal anisotropy direction, this has not been observed in the particles with relatively high porosities.

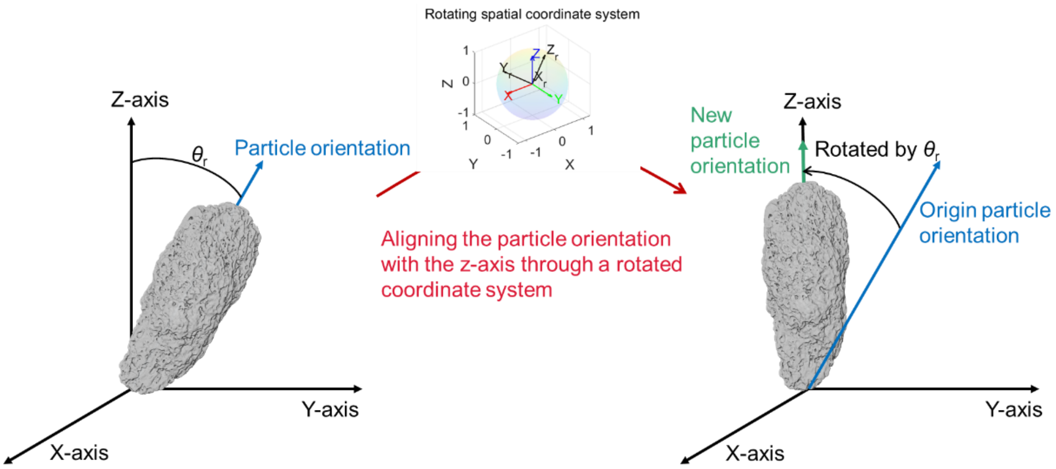

Fig. 6 Schematic diagram of a particle in the rotating coordinate system

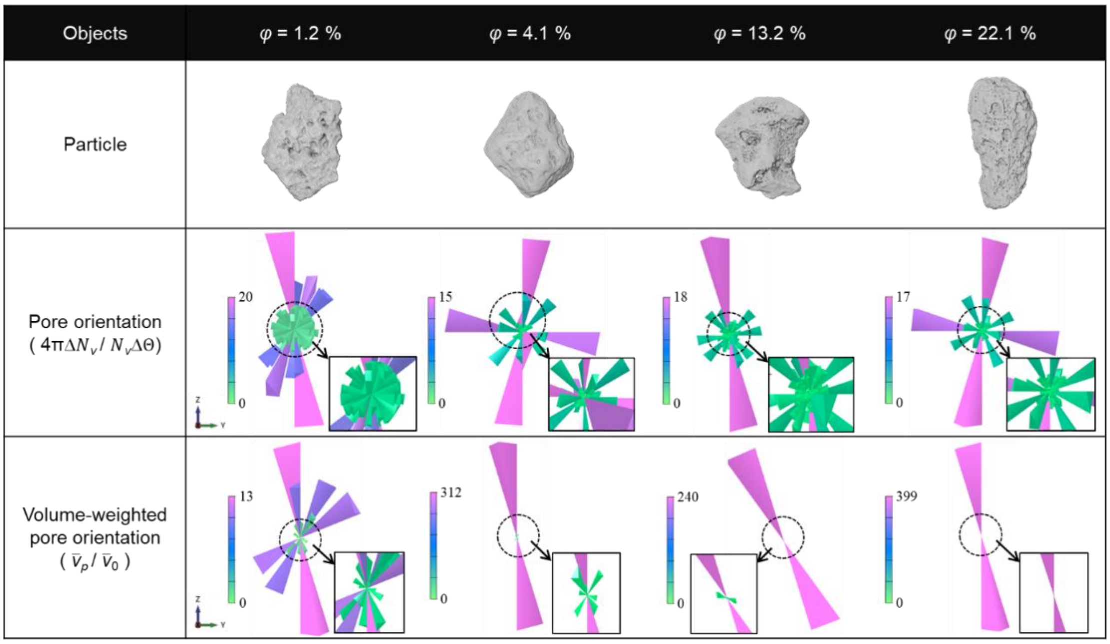

Fig. 7 3D histograms of the pore orientation of particles with different porosity

The pore distribution anisotropy magnitude, given by the invariants a_p and a_v (where a_p denotes the pore orientation anisotropy intensity and a_v represents the volume-weighted pore orientation anisotropy intensity, as defined in Eq. 8), is plotted in Fig. 8. It is seen that the a_v is obviously higher than a_p, indicating that the distribution of volume-weighted pore orientation vectors has a significantly higher anisotropy degree than that for the pure pore orientation vector. Both a_p and a_v demonstrate highly non-normal distribution characteristics. Interestingly, the Johnson distribution can basically more accurately capture the main skewness-kurtosis region, providing a better fit of the pore anisotropy magnitude than the normal distribution. Furthermore, a particle-size dependence of anisotropy magnitude is observed in a_v, and larger particles tend to possess higher a_v values.

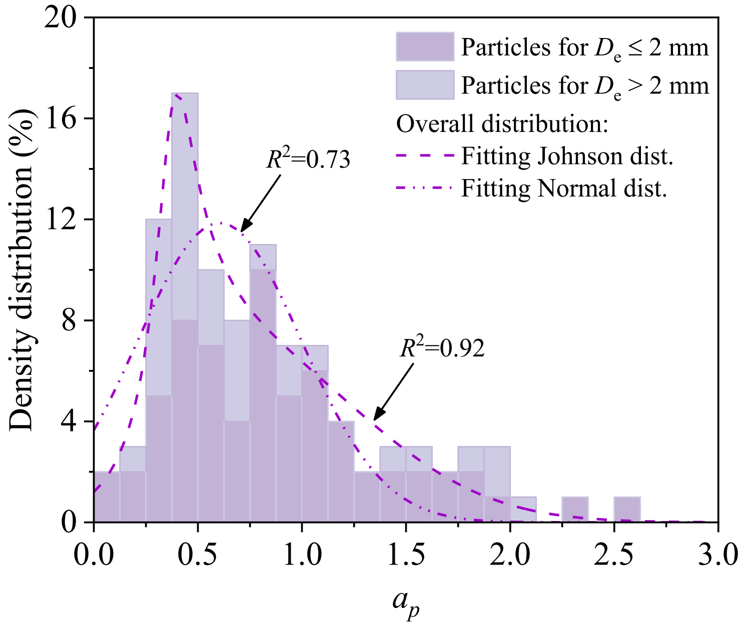

(a)

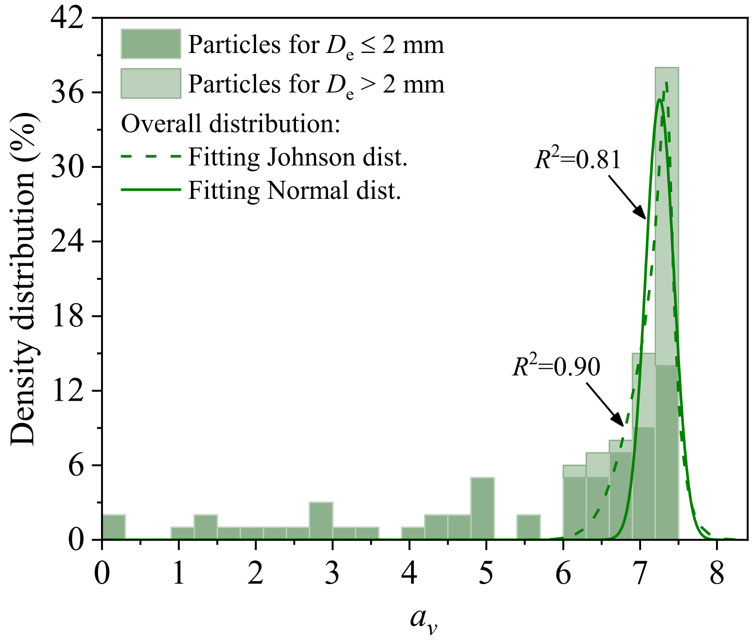

(b)

Fig. 8 Distributions of (a) a_p and (b) a_v for the tested carbonate sand particles

To explore more fundamentals of the spatial distribution of pore structures, the internal pores are classified into open and closed pores. The open pores can directly interact with the external fluids, but the closed pores cannot (Rouquerol et al. 1994; Zhou et al. 2021). In this study, a special algorithm was utilized to differentiate the closed pores from the overall internal pores by picking up the pore voxels surrounded by the solid voxels. As illustrated in Fig. 9(a), this algorithm operates within a three-dimensional space, where a voxel as a void phase (with the point value 0) is identified as a closed pore if all 26 neighboring voxels are labeled as the solid phase (with the point value 1), and 34 neighboring solid voxels in total are needed to be evaluated to identify two voxels of closed pores. Fig. 9(b) provides a comparison of porosity attributed to closed pores and open pores for a typical particle (see Fig. 9(c)), with their corresponding visualizations displayed in Figures 9(d) and 9(e). It can be seen that open pores are substantially larger than closed pores, thus accounting for the majority of the total internal pore volume. Notably, some open pores may appear as closed pores in 2D slices; however, in 3D space, these pores are actually connected to the particle's external surface. Fig. 10 shows the variations of the anisotropy magnitudes of a_p and a_v for different pore types, with the general variation trends characterized by the Johnson distribution fitting curves. It is interesting to see that a_v for the open pores is comparable to that for overall pore entities, whereas a_v for the closed pores is distinctly lower. Since a_v has incorporated the influence of pore volume, the similarity in the distribution anisotropy between the open pores and the overall pores suggests that open pores comprise a significant volume fraction of the entire internal pore structure. The peak point of the fitting curve, denoted as $a_{*,p}$, represents the maximum occurrence probability at a particular anisotropy magnitude which is 0.395 for a_p and 7.336 for a_v across all internal pores.

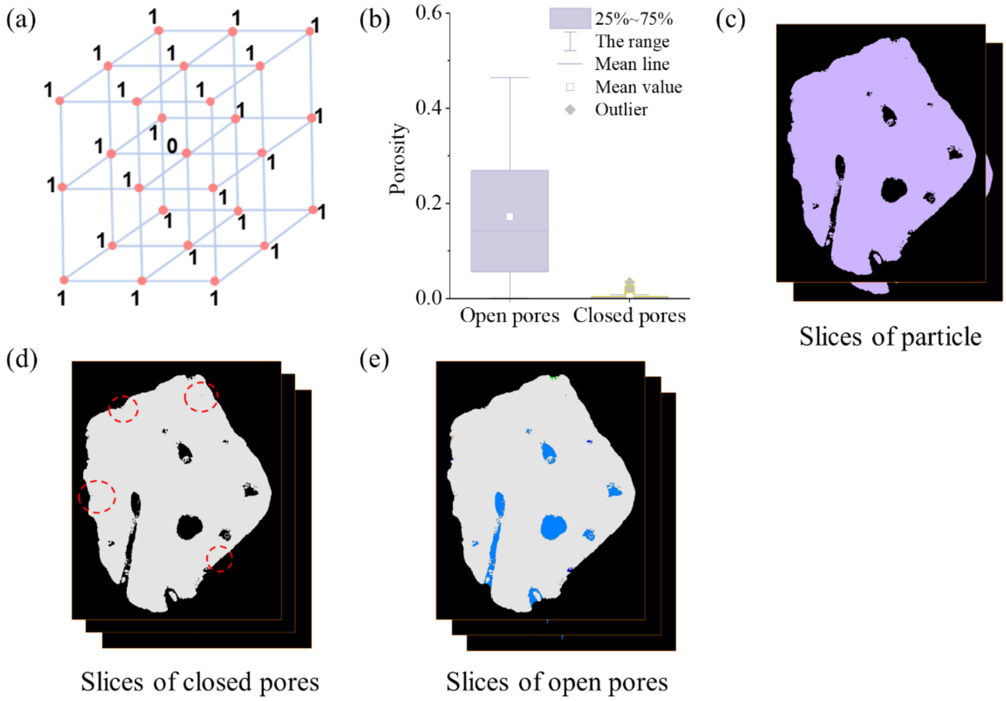

Fig. 9 (a) Definition of closed pores in digital images. (b) Boxplot illustrating the porosity associated with open pores and closed pores for tested carbonate sand particles. (c) Slices of the particle skeleton for a typical particle. (d-e) Visualizations of closed pores and open pores. The colors in the slices present the pixel of pore regions, and the white color in (d-e) presents the particle skeleton boundary.

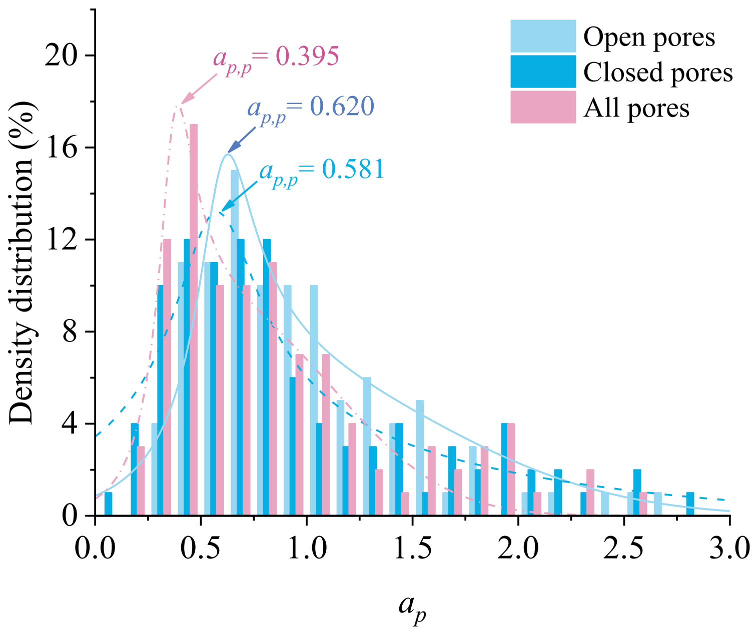

(a)

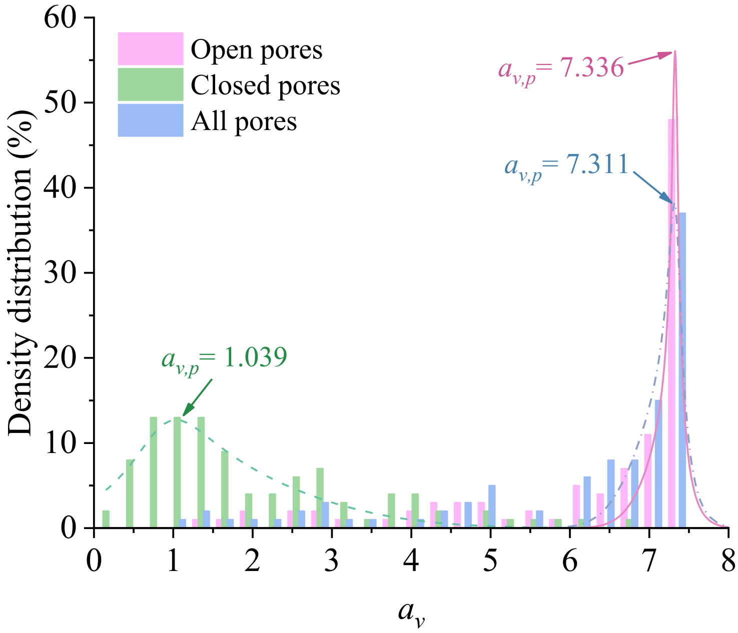

(b)

Fig. 10 Variation of (a) a_p and (b) a_v with respect to different pore types

4.3 Correlation of pores and particle skeleton parameters

Fig. 11 plots the anisotropy magnitudes against the porosity with respect to different types of pores. It is observed that the anisotropy parameter a_p does not have a close correlation with the porosity for both open pores and overall pores. But, a_v for open pores and overall pores exhibits an increasing trend with the increasing porosity, and eventually converges to a limit value of 7.5 as estimated by Eqs. (7) and (8). This is because the pore network in a particle tends to exhibit a greater connectivity as the porosity increases, with a good number of relatively small pores more likely to coalesce into a relatively large pore, rather than remaining individually isolated. These coalesced large pore structures usually have a greater volume and dominate the impact on the principal anisotropy direction of the volume-weighted pore orientation vectors. In this connection, particles with a high porosity (> 0.3) exhibit an extremely high degree of volume-weighted pore anisotropy. Additionally, Fig. 11 shows that the variation of anisotropy magnitudes for the open pores and overall pores are similar to each other, meaning that the internal pores are primarily composed of open pores, and the closed pores may constitute only a small fraction of the total pore volume.

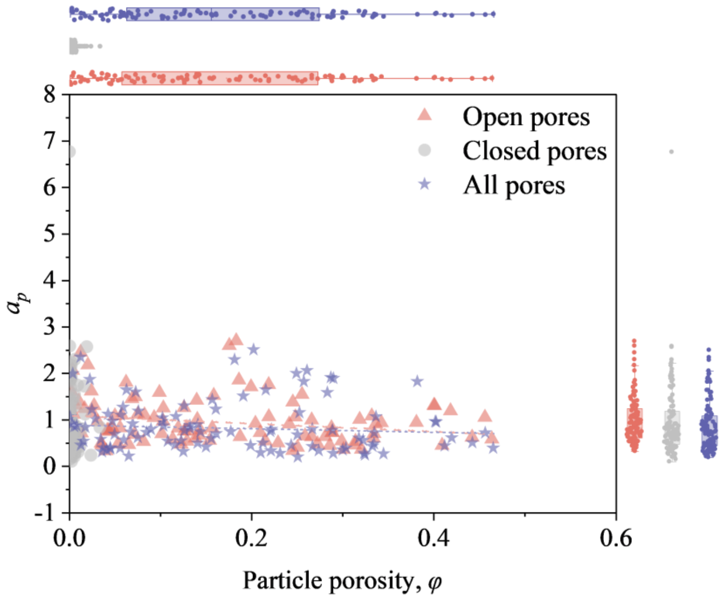

(a)

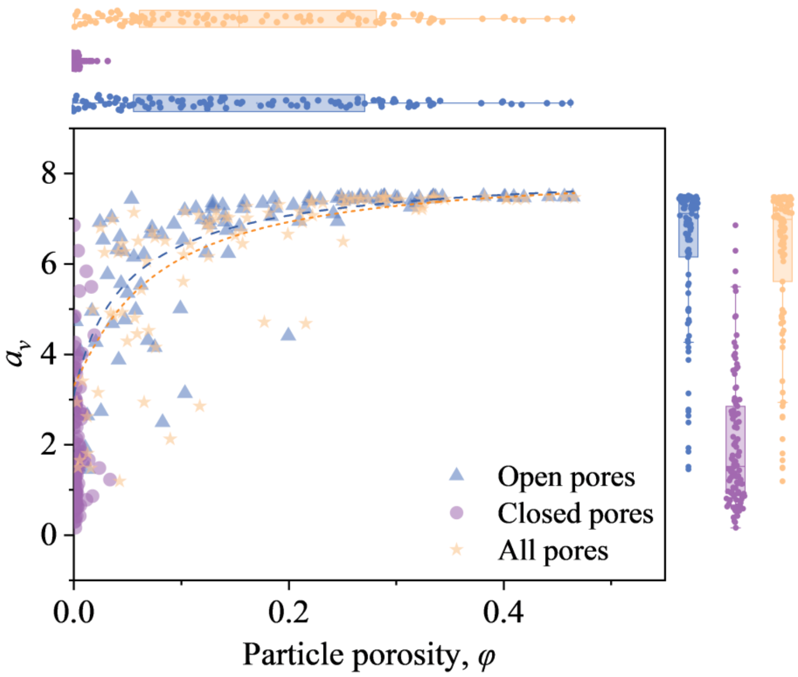

(b)

Fig. 11 Variation in anisotropy degrees for different pore types: (a) a_p and (b) a_v

To probe the correlation between the pore distribution anisotropy and the solid particle skeleton, the angle θ^*, defined as the angle formed between the particle's long axis and the principal anisotropy direction for volume-weighted pore orientation vectors, is plotted against the particle porosity as shown in Fig. 12. It is observed that as the particle porosity increases, θ^* tends to decrease towards zero, with the distribution range narrowing, particularly for the particles with D_e > 2 mm. For particles having a low porosity, the pore structure in them may consist of many small pores, resulting in a relatively random pore orientation distribution and a lower anisotropy degree (see Fig. 7). However, for carbonate sand particles of high porosity, a large and highly connected pore structure (depicted in blue) typically dominates the volume of intra-particle pore phase. This large pore structure is an open pore, featuring a large amount of inner channels connected to the exterior surface of particles and exhibiting to some extent the external contour characteristics of the particle's solid skeleton. This has led to a high consistency between the particle orientation and the principal anisotropy direction for the volume-weighted pore orientation vectors.

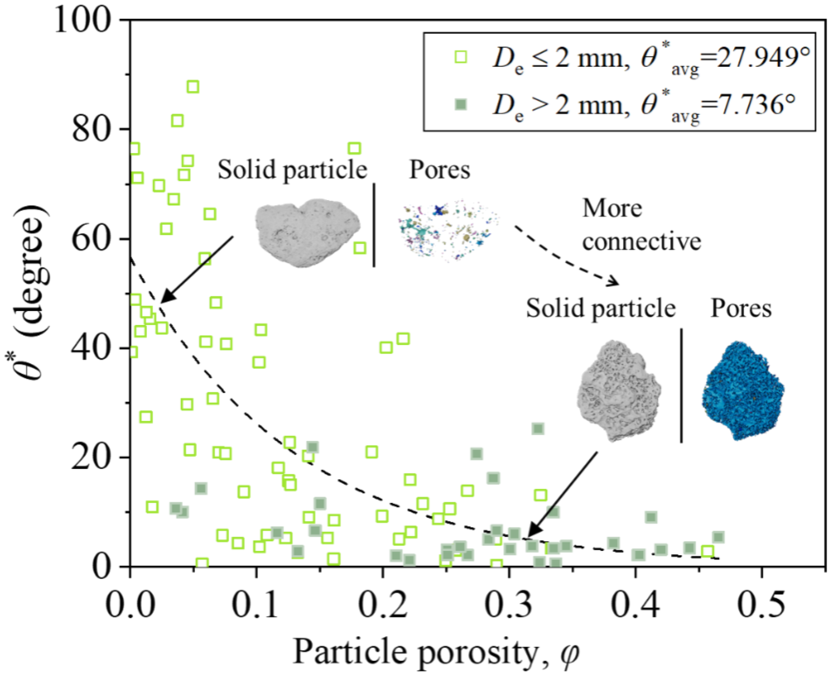

Fig. 12 Variation in anisotropy degrees for different pore types: (a) a_p and (b) a_v

Various correlation coefficients can be employed to analyze the relationships between parameters, including Pearson and Spearman coefficients. The Spearman rank correlation coefficient effectively characterizes both linear and nonlinear correlations, whereas the Pearson coefficient is only suitable for representing linear correlations. Therefore, the Spearman rank correlation is here used to further analyze the relations of the pore characteristics parameters with the descriptive parameters of particle skeleton morphology, which is expressed as follows

$$\rho_{Spearman} = 1 - \frac{6\sum d_i^2}{n\left(n^2 - 1\right)} \tag{11}$$

where $\rho_{Spearman}$ is the Spearman rank correlation coefficient, d_i (= x_i - y_i) is the difference between two ranks of each observation, n is the number of observations. The heat map of Spearman correlation coefficients is shown in Fig. 13, where the degree of correlation between two characteristic indexes is represented by the red and blue colors in each cell, with red denoting a positive correlation and blue referring to a negative correlation. Notably, a strong positive correlation is observed between the particle porosity and the anisotropy parameter a_v. As both porosity and a_v increase, the anisotropy parameter θ^* tends to decrease, indicating a complex interplay between the particle morphology and the anisotropy. Moreover, the sphericity, a key descriptor of particle shape, shows a significant negative correlation with the porosity and it is also related to a_v and θ^*, which reveals the connection between the characteristics of the solid and pore phases in carbonate sand particles. The accompanying bar chart indicates that the Spearman coefficient is generally higher than the Pearson coefficient for most parameters, with some exceptional cases such as the coefficient difference between *EL* and *AR*. However, it is important to note that although the anisotropy parameter a_v shows relatively high correlations with several important parameters, they are not strictly interdependent. This is because a_v is influenced by the presence of a large and highly connected pore structure in the particle, and the degree of such correlations depends on the particle size.

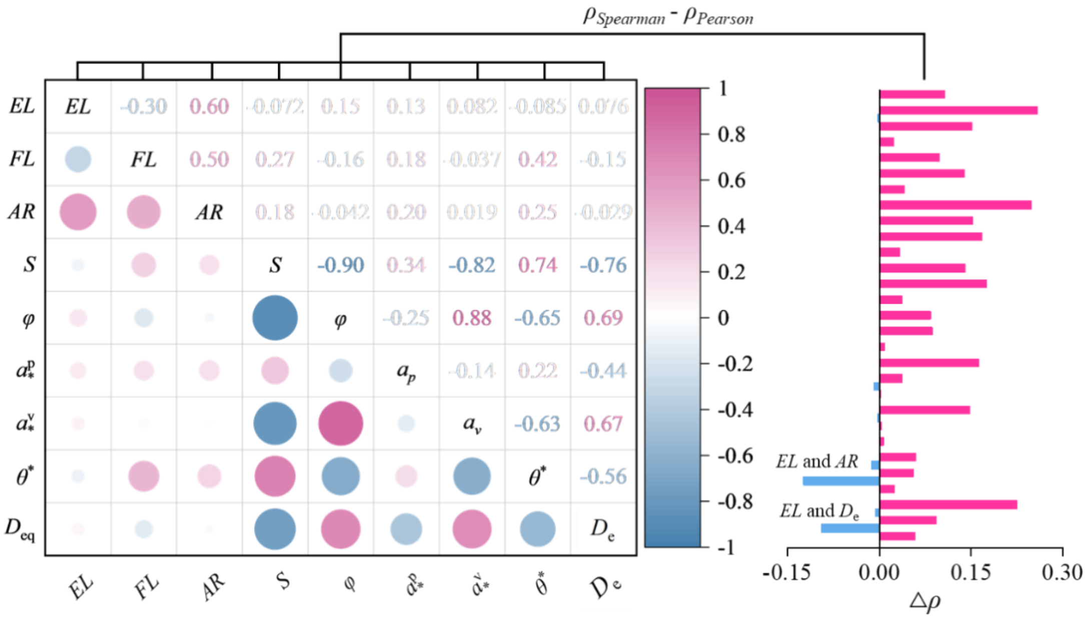

Fig. 13 Variation of Spearman correlation coefficients between different features

4.4 Pore permeability

The mechanical behavior of granular assembly depends on the rearrangement of discrete particles in a particular mechanical process, which is accompanied by the variation of inter-particle pores. Also, the permeability of granular assembly is decided by the presence of inter-particle voids. But the influence of intra-particle pores should also not be overlooked, as they affect single-particle properties such as permeability, mechanical strength, and deformation behavior. To further explore this aspect, Fig. 14(a) presents the relationship between a_v and absolute permeability for carbonate sand particles. The permeability of each particle is calculated using the pore network model (PNM) (see Figs. 14b and 14c). The PNM simplifies the complex pore structure into a network of interconnected pores and throats, enabling efficient simulation of fluid flow through porous media. This method has been demonstrated to effectively predict transport properties in previous studies (Zhang et al. 2022; Zhou et al. 2020). In the flow simulation, the input pressure and the output pressure are set at 130 kPa and 100 kPa, respectively. The results indicate that for particles with a_v values lower than 6.4, the permeability of particles has minimal influence on the overall fluid transport of an assembly, due to the weak connectivity of internal pores (see Fig. 14b). In contrast, particles with high a_v values (>6.4) exhibit a more interconnected pore network (see Fig. 14c), which facilitates fluid flowing through the particles. In this case, the internal pores would lead to the occurrence of the phenomenon described by Zhou et al. (2023); that is, fluid can permeate the carbonate sand particle even at low seepage pressures. The presence of open pores is found to increase the overall permeability of particle assemblies (Li et al. 2023), and as pore orientation depends on the particle direction (see Fig. 12), variations in particle fabric can introduce complex effects on the fluid transport properties of the assembly.

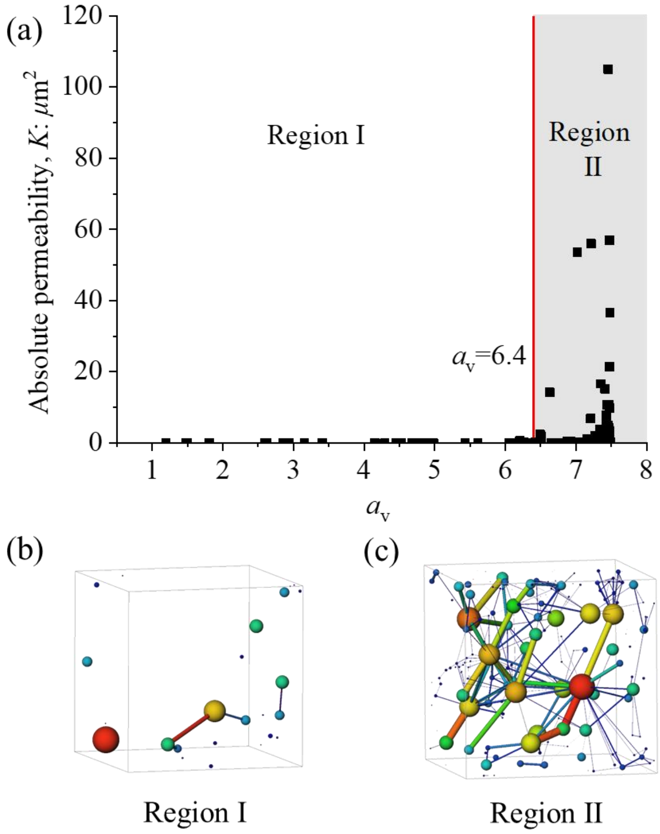

Fig. 14 (a) Relationship between a_v and permeability. (b-c) PNM model for typical carbonate sand particles in different regions. In the PNM, spheres represent individual pores, while sticks represent the throats connecting the pores. The color gradient indicates pore volume, with red denoting larger volumes and blue representing smaller volumes.

5. Conclusion

This study attempts to characterize the spatial distribution of internal pore structures of carbonate sand particles by carrying out the X-ray CT scanning experiments. A vector representation approach is proposed in the framework of statistical micromechanics for the description of pore structures. The major findings are summarized as follows.

1. The pore orientation vector, as well as the volume-weighted pore orientation vector,

is proposed to describe the spatial distribution of intra-particle pores, and is also used to micromechanically formulate a tensor which characterizes the anisotropic distribution of internal pore structures.

2. The anisotropy magnitude of volume-weighted pore orientation vectors is considerably higher than that of pure pore orientation vectors for the carbonate sand particles concerned in this study. For the particles with high porosities, the anisotropic distribution of volume-weighted pore orientation vectors is mainly influenced by the presence of a large open pore that takes up most of the pore space, which makes a_v approximate to the maximum value and principal pore anisotropy direction be close to the particle orientation. For particles with a_v greater than 6.4, the impact of internal pore permeability on the overall hydraulic transport behavior of the particle assembly needs further attention.
3. The unique pore structure characteristics of carbonate sand particles exhibit certain relationships with the particle skeleton morphology. However, some correlations, such as those between the sphericity and the porosity and pore anisotropy, are not strictly interdependent, depending on some specific particle characteristics, such as the pore connectivity and size.
4. The porosity, pore diameter, and anisotropy parameter a_v all exhibit a dependence on particle size, whereas pore shape parameter (i.e., aspect ratio) does not. The Johnson distribution function is suitable for fitting skewness-kurtosis pore parameter data, while the Gaussian distribution function is more appropriate for symmetrical distributions.

Data Availability Statement

Some or all data, models, or codes that support the findings of this study are available from the corresponding author upon reasonable request.

Acknowledgments

This work was supported by the National Natural Science Foundation of China (Nos. 52078507, 42472343), the Natural Science Foundation of Guangdong Province (No. 2024A1515011019), and the China Scholarship Council (CSC) (202406380191).

Reference

Andò, E., Viggiani, G., Hall, S. A., and Desrues, J. (2013). Experimental micro-mechanics of granular media studied by X-ray tomography: recent results and challenges. *Géotechnique Letters*, 3(3), 142-146.

Cheng, Z., and Wang, J. (2021). An investigation of the breakage behaviour of a pre-crushed carbonate sand under shear using X-ray micro-tomography. *Engineering Geology*, 293, 106286.

Coop, M. R. (1990). The mechanics of uncemented carbonate sands. *Géotechnique*, 40(4), 607-626.

Dong, Z.-L., Cheng, Y. P., Tong, C.-X., Liu, H., Zhang, S., and Sheng, D. (2024). DEM modelling of particle crushing of single carbonate sand using the improved bonded particle model. *Powder Technology*, 445, 120121.

Fan, Z., Hu, C., Zhu, Q., Jia, Y., Zuo, D., and Duan, Z. (2021). Three-dimensional pore characteristics and permeability properties of calcareous sand with different particle sizes. *Bulletin of Engineering Geology and the Environment*, 80, 2659-2670.

Fonseca, J., O'sullivan, C., COOP, M. R., and Lee, P. (2013). Quantifying the evolution of soil fabric during shearing using directional parameters. *Géotechnique*, 63(6), 487-499.

Fonseca, J., O'Sullivan, C., Coop, M. R., and Lee, P. (2012). Non-invasive characterization of particle morphology of natural sands. *Soils and Foundations*, 52(4), 712-722.

Gao, Q.-F., Jrad, M., Hattab, M., Fleureau, J.-M., and Ameur, L. I. (2020). Pore morphology, porosity, and pore size distribution in kaolinitic remolded clays under triaxial loading. *International Journal of Geomechanics*, 20(6), 04020057.

Giretti, D., Been, K., Fioravante, V., and Dickenson, S. (2018). CPT calibration and analysis for a carbonate sand. *Géotechnique*, 68(4), 345-357.

Guo, N., and Zhao, J. (2013). The signature of shear-induced anisotropy in granular media. *Computers and Geotechnics*, 47, 1-15.

Hardin, B. O. (1985). Crushing of soil particles. *Journal of geotechnical engineering*, 111(10), 1177-1192.

He, S.-H., Ding, Z., Hu, H.-B., and Gao, M. (2021). Effect of grain size on microscopic pore structure and fractal characteristics of carbonate-based sand and silicate-based sand. *Fractal and Fractional*, 5(4), 152.

Huang, S., Huang, L., Lai, Z., and Zhao, J. (2023). Morphology characterization and discrete element modeling of coral sand with intraparticle voids. *Engineering Geology*, 315, 107023.

Johnson, N. L. (1949). Systems of frequency curves generated by methods of translation. *Biometrika*, 36(1/2), 149-176.

Karatza, Z., Ando, E., Papanicolopulos, S.-A., Ooi, J., and Viggiani, G. (2018). Evolution of deformation and breakage in sand studied using X-ray tomography. *Géotechnique*, 68(2), 107-117.

Ken-Ichi, K. (1984). Distribution of directional data and fabric tensors. *International journal of engineering science*, 22(2), 149-164.

Kong, D., and Fonseca, J. (2018). Quantification of the morphology of shelly carbonate sands using 3D images. *Géotechnique*, 68(3), 249-261.

Krumbein, W. C. (1941). Measurement and geological significance of shape and roundness of sedimentary particles. *Journal of Sedimentary Research*, 11(2), 64-72.

Kuang, D.-m., Long, Z.-l., Ogwu, I., Kuang, F.-l., and Yang, L.-m. (2024). DEM study on the effect of pore characteristic on single particle crushing behavior of porous articles. *Computers and*

Geotechnics, 165, 105919.

Li, H., Chai, H., Xiao, X., Huang, J., and Luo, S. (2020). Fractal breakage of porous carbonate sand particles: Microstructures and mechanisms. *Powder Technology*, 363, 112-121.

Li, Y., Guo, Z., Wang, L., and Yang, H. (2023). A coupled bio-chemo-hydro-wave model and multi-stages for MICP in the seabed. *Ocean Engineering*, 280, 114667.

Lv, Y., Li, X., Fan, C., and Su, Y. (2021). Effects of internal pores on the mechanical properties of marine calcareous sand particles. *Acta Geotechnica*, 16(10), 3209-3228.

Ma, G., Chen, Y., Yao, F., Zhou, W., and Wang, Q. (2019). Evolution of particle size and shape towards a steady state: Insights from FDEM simulations of crushable granular materials. *Computers and Geotechnics*, 112, 147-158.

Ma, G., Zhou, W., and Chang, X.-L. (2014). Modeling the particle breakage of rockfill materials with the cohesive crack model. *Computers and Geotechnics*, 61, 132-143.

Ma, X., Jiang, J., Zhao, Y., and Wang, H. (2021). Characterization of the interconnected pore and its relationship to the directional permeability of porous asphalt mixture. *Construction and Building Materials*, 269, 121233.

Nishimura, I., Yabiku, Y., Shinyama, Y., Mukunoki, T., and Matsubara, H. (2024). CT image-based simulation of microbially induced carbonate precipitation. *Computers and Geotechnics*, 174, 106651.

Otsu, N. (1979). A threshold selection method from gray-level histograms. *IEEE Trans SMC*, 9, 62.

Ouadfel, H., and Rothenburg, L. (2001). Stress–force–fabric'relationship for assemblies of ellipsoids. *Mechanics of materials*, 33(4), 201-221.

Rouquerol, J., Avnir, D., Everett, D., Fairbridge, C., Haynes, M., Pernicone, N., Ramsay, J., Sing, K., and Unger, K. (1994). Guidelines for the characterization of porous solids. *Studies in surface science and catalysis*, Elsevier, 1-9.

Rouquerol, J., Avnir, D., Fairbridge, C. W., Everett, D. H., Haynes, J., Pernicone, N., Ramsay, J. D., Sing, K. S. W., and Unger, K. K. (1994). Recommendations for the characterization of porous solids (Technical Report). *Pure and applied chemistry*, 66(8), 1739-1758.

Satake, M. Fabric tensor in granular materials. *Proc., IUTAM-Conference on Deformation and Failure of Granular Materials, 1982*, 63-68.

Sitharam, T., Vinod, J., and Ravishankar, B. (2009). Post-liquefaction undrained monotonic behaviour of sands: experiments and DEM simulations. *Géotechnique*, 59(9), 739-749.

Sun, Q., and Zheng, J. (2019). Two-dimensional and three-dimensional inherent fabric in cross-anisotropic granular soils. *Computers and Geotechnics*, 116, 103197.

Titschack, J., Baum, D., Matsuyama, K., Boos, K., Färber, C., Kahl, W.-A., Ehrig, K., Meinel, D., Soriano, C., and Stock, S. R. (2018). Ambient occlusion–A powerful algorithm to segment shell and skeletal intrapores in computed tomography data. *Computers & Geosciences*, 115, 75-87.

Wu, Y., Dai, B., Xu, K., Liu, P., Wu, Y., and Liu, J. (2024). Particle-morphology-based characterization of the breakage behavior of particle assemblies under one-dimensional compression. *Acta Geotechnica*, 1-18.

Zhang, J., Ma, G., Yang, Z., Ma, Q., Zhang, W., and Zhou, W. (2022). Investigation of flow characteristics of landslide materials through pore space topology and complex network analysis. *Water Resources Research*, 58(9), e2021WR031735.

Zhang, X., Zhou, B., You, L., Wu, Z., and Wang, H. (2023). Cementation anisotropy associated with microbially induced calcium-carbonate precipitation and its treatment effect on calcareous and quartz sands. *Construction and Building Materials*, 395, 132237.

Zhao, B., Wang, J., Coop, M., Viggiani, G., and Jiang, M. (2015). An investigation of single sand particle fracture using X-ray micro-tomography. *Géotechnique*, 65(8), 625-641.

Zhao, C.-F., Pinzón, G., Wiebicke, M., Andò, E., Kruyt, N. P., and Viggiani, G. (2021). Evolution of fabric anisotropy of granular soils: X-ray tomography measurements and theoretical modelling. *Computers and Geotechnics*, 133, 104046.

Zhao, S., Evans, T. M., and Zhou, X. (2018). Shear-induced anisotropy of granular materials with rolling resistance and particle shape effects. *International Journal of Solids and Structures*, 150, 268-281.

Zheng, Y., Baudet, B. A., Delage, P., Pereira, J.-M., and Sammonds, P. (2022). Pore changes in an illitic clay during one-dimensional compression. *Géotechnique*, 73(10), 917-932.

Zhou, B., Ku, Q., Li, C., Wang, H., Dong, Y., and Cheng, Z. (2022). Single-particle crushing behaviour of carbonate sands studied by X-ray microtomography and a combined finite–discrete element method. *Acta Geotechnica*, 1-15.

Zhou, B., Ku, Q., Wang, H., and Wang, J. (2020). Particle classification and intra-particle pore structure of carbonate sands. *Engineering Geology*, 279, 105889.

Zhou, B., Zhang, X., Wang, J., Wang, H., and Shen, J. (2023). Insight into the mechanism of microbially induced carbonate precipitation treatment of bio-improved calcareous sand particles. *Acta Geotechnica*, 18(2), 985-999.

Zhou, M., Li, J., Luo, Z., Sun, J., Xu, F., Jiang, Q., and Deng, H. (2021). Impact of water–rock interaction on the pore structures of red-bed soft rock. *Scientific Reports*, 11(1), 7398.

Zhou, W., and Xu, M. (2024). Microscopic analysis of the nonlinear stiffness of granular materials at small-to-medium strain. *Computers and Geotechnics*, 165, 105859.

Table 1. Pore characterization parameter distributions using Johnson's fitting method

Distribution parameters	ξ	δ	λ	γ	R^2
Porosity, φ	-0.059	3.712	0.018	-0.887	0.83
Pore orientation anisotropy, a_p	0.377	10.299	0.096	-1.380	0.92
Volume-weighted pore orientation anisotropy, a_v	7.355	13.745	0.089	1.038	0.90